

# Effects of nutrient depletion on tissue growth in a tissue-engineering scaffold pore

Zeshun Zong (宗泽舜)<sup>1, a)</sup> Xinyu Li (李新宇)<sup>2, a)</sup> and Pejman Sanaei<sup>3, b)</sup>

<sup>1)</sup> *Mathematics Department, University of California, Los Angeles, Los Angeles, CA 90095-1555, USA*

<sup>2)</sup> *Industrial Engineering and Operations Research, University of California, Berkeley, Berkeley, CA 94720-5800, USA*

<sup>3)</sup> *Department of Mathematics, New York Institute of Technology, New York, NY 10023-7692, USA*

(Dated: 1 November 2021)

In a tissue-engineering scaffold pore lined with cells, nutrient-rich culture medium flows through the scaffold and cells proliferate. In this process, both environmental factors such as flow rate, shear stress, as well as cell properties have significant effects on tissue growth. Recent studies focused on effects of scaffold pore geometry on tissue growth, while in this work, we focus on the nutrient depletion and consumption rate by the cells, which cause a change in nutrient concentration of the feed and influence the growth of cells lined downstream. In this paper, our objectives are threefold: (i) design a mathematical model for the cell proliferation describing fluid dynamics, nutrient concentration, and tissue growth; (ii) solve the models and then simulate the tissue proliferation process; (iii) design a “reverse algorithm” to find the initial configuration of the scaffold with the knowledge of the desired property of the final tissue geometry. Our model reduces the numerical burdens and captures the experimental observations from the literature. In addition, it provides an efficient algorithm to simulate the cell proliferation and determine the design of a tissue engineering scaffold given a desired tissue profile outcome.

## I. INTRODUCTION

Tissue engineering, which is culturing artificial tissue outside human body in order to replace damaged tissues and organs, has been widely used for clinical therapies<sup>1,2</sup>. In this process, both environmental factors such as flow rate, shear stress, and the cell property have significant effects on tissue growth. Previous works have discussed the effects of external factors on tissue growth, including fluid mechanical forces with a focus on shear stress and pressure<sup>3-6</sup>, as well as the scaffold geometric design<sup>7-11</sup>. In addition, many mathematical models of tissue growth have been built to provide simulations on the final shape and the pore-filling process<sup>12,13</sup>. While most of the focus has been devoted to the influences brought by the external environment such as the fluid dynamics and the scaffold geometric design, less attention has been drawn onto the effects of cells’ behavior. Note that, as cells consume the nutrient, nutrient concentration in the flow changes. In particular, as cells at the top of the scaffold pore consume nutrients, the concentration of nutrient solution will be lower at the bottom of the scaffold pore, which in turn results in a slower growth rate for cells at the downstream side. Therefore, both the final scaffold pore geometry and the total amount of the tissue growth are influenced. Previous works did not reveal the influence of this factor<sup>7,14,15</sup>.

Numerous mathematical models have been developed by researchers to study the cell proliferation in a tissue engineering scaffold. For example, Kumar *et al.*<sup>16,17</sup> introduced models for deformable cylindrical scaffold and neglected the effects of nutrient depletion along the depth of the scaffold. In addition, the researchers<sup>17</sup> provided a semi-analytical solution for a short period of time. Sanaei *et al.*<sup>14</sup> proposed a mathematical model for tissue engineering in the context of a single pore of a scaffold. The authors considered the combined roles of fluid shear stress and geometry curvature of a scaffold pore on the tissue growth and investigated how these factors influence the total tissue growth in a scaffold pore. A critical assumption of all of the mentioned works above<sup>7,14-17</sup> is that the nutrient concentration is assumed to be constant throughout the scaffold pore. In reality, however, the assumption does not hold. As cells begin to consume the nutrient, the concentration decreases and influences the cells’ growth rate at the downstream side of the scaffold. In this work, we develop a model and introduce a parameter named “hunger rate” to determine the homogeneous nutrient depletion rate of cells in the tissue engineering scaffold. We focus on the homogeneous property of cells in the scaffold and assume that each individual cell in the scaffold would consume the nutrient at the same hunger rate. In this way, we are able to compare the final geometries and the growth processes of different kinds of cells with different hunger rates.

Another innovative part of our work is the implementation a “reverse algorithm,” which is used to design the initial configuration of the tissue engineering scaffold. Though there are several mathematical models to predict the tissue growth process and provide spatio-temporal in-

---

<sup>a)</sup>These authors contributed equally to this work.

<sup>b)</sup>Electronic mail: [psanaei@nyit.edu](mailto:psanaei@nyit.edu); <https://sites.google.com/nyit.edu/pejman-sanaei-webpage>

formation on the scaffold pore final shape<sup>14,18,19</sup>, very few have devoted on designing the tissue engineering scaffold (see<sup>20–23</sup> and references therein). They mostly used comprehensive parametric variation study to design and optimize the tissue engineering scaffold. Specifically, what is missing from the literature is a model adopting a predictive algorithm using first principles for optimizing and designing the initial configuration of the tissue engineering scaffold based on the final desired tissue geometry. For a practical use however, a correct initial configuration of the scaffold could be very critical<sup>8,24</sup>. In this work, we also design an algorithm to reverse the growth process of cells, starting from the final desired tissue geometry, and to find out the corresponding initial scaffold design. By incorporating the nutrient concentration and fluid dynamics, the algorithm is able to return a precise 3-dimensional scaffold design efficiently.

This paper is structured as the following: in §II, we introduce the mathematical model incorporating three parts: the governing equations for fluid dynamics through a single pore of a tissue engineering scaffold in §II A; the rate of change of the nutrient concentration and its boundary conditions in §II B; the partial derivative equations governing the tissue growth in §II C. We perform the non-dimensionalization of the models in §III and then apply asymptotic and quasi-static analysis to solve the PDE systems in §IV, where we utilize the fact that the aspect ratio of the pore is small and the time scale of cell proliferation is much longer compared to that of nutrient flow transport. The results are shown in §V and we present the reverse algorithm and initial configuration. Finally, we conclude in §VI with a discussion of our model and results with potential future improvements.

## II. MODEL DESCRIPTION

We consider a simple continuum model, in which the scaffold consists of a series of identical nearly cylindrical pores spanning the entire scaffold, with depth-dependent radius shown in Fig 1. Therefore, we focus on a single scaffold pore, with cells initially lined on the pore wall and nutrient solution flows through the pore. As time passes, the cells proliferate and the fluid-cell-layer shrinks as the tissue layer thickens. As a result, the shape and structure of the pore changes, so do the concentration of nutrient, shear stress, etc. We consider a quasi-static assumption, which stems from the fact that the tissue growth happens on a much longer timescale compared to that of the transport of the fluid flow through the scaffold pore<sup>8,14</sup>.

Since the shape of the scaffold is fixed throughout the paper, we primarily consider the change of the shape of fluid-cell-layer, which represents the growth of tissue. Let  $\hat{L}$  and  $\hat{R}$  denote the length and the typical pore radius respectively; hence also the length and radius of fluid-cell-layer at the initial state, since we assume initially

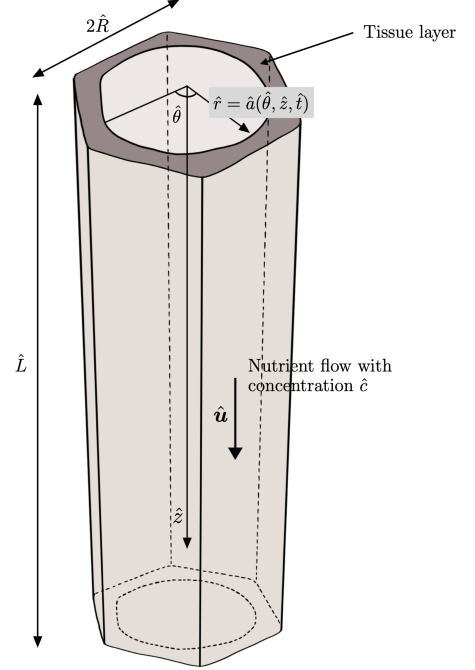


FIG. 1. Schematic diagram of a possible geometry of a tissue-lined pore within a tissue engineering construct.

the thickness of cell sources is negligible. The aspect ratio  $\epsilon$  is defined to be  $\epsilon = \hat{R}/\hat{L} \ll 1$ . The geometry of the underlying substrate is assumed to be nearly circularly cylindrical with small azimuthal and axial variation, which later would be viewed as a control for optimization of the tissue growth.

The concentration of nutrient solution is allowed to change throughout the length of pore, due to nutrient consumption by the cells at the pore wall. We assume, as in many real world applications, the inlet flux and concentration of fluid supplied to the cells is held at constant<sup>25,26</sup>. Intuitively, if the rate of nutrient consumption is low, which we will characterize it by the “hunger rate”  $\hat{\eta}$ , then our model should resemble the case considered in<sup>14</sup> that the nutrient is in excess. As is in<sup>14</sup>, we prescribe the influx  $\hat{Q}_i$  and zero downstream pressure. The nutrient fluid is modeled as an incompressible Newtonian viscous fluid with viscosity  $\hat{\mu}$  and density  $\hat{\rho}$ .

The system is constructed in cylindrical coordinates  $(\hat{r}, \theta, \hat{z})$ , where the vertical axis  $\hat{z}$  is aligned with the pore axis and  $\mathbf{e}_{\hat{r}}, \mathbf{e}_{\theta}, \mathbf{e}_{\hat{z}}$  be the unit vectors in  $\hat{r}, \theta, \hat{z}$  directions respectively. Let  $\hat{r} = \hat{a}(\theta, \hat{z}, \hat{t})$  describes the fluid-cell-layer interface, where the initial configuration is given by  $\hat{r} = \hat{a}(\theta, \hat{z}, 0)$  as shown in Fig 1.

### A. Fluid dynamics

We denote the velocity of the fluid and the pressure across the pore as  $\hat{\mathbf{u}} = \hat{u}_{\hat{r}}\mathbf{e}_{\hat{r}} + \hat{v}_{\theta}\mathbf{e}_{\theta} + \hat{w}_{\hat{z}}\mathbf{e}_{\hat{z}}$  and  $\hat{p}$ , respectively.

Experiments and literatures have shown that the inertial force is negligible<sup>27,28</sup>, therefore, we assume that the flow is governed by the Stokes equations subject to no slip and no penetration boundary conditions. Mechanics of the flow are therefore characterized by

$$\hat{\nabla} \hat{p} = \hat{\mu} \hat{\nabla}^2 \hat{\mathbf{u}}, \quad \hat{\nabla} \cdot \hat{\mathbf{u}} = 0, \quad (1)$$

with boundary conditions

$$\hat{\mathbf{u}}|_{\hat{r}=\hat{a}} = 0, \quad \hat{u}|_{\hat{r}=0} = \hat{v}|_{\hat{r}=0} = \left. \frac{\partial \hat{w}}{\partial \hat{r}} \right|_{\hat{r}=0} = 0, \quad (2)$$

where  $\hat{\nabla}$  is the dimensional gradient operator. Throughout the procedure, we assume that the total flux passing through the pore is held constant to keep a continued nutrient supply, *i.e.*

$$\int_0^{2\pi} \int_0^{\hat{a}} |\hat{\mathbf{u}}| \hat{r} d\hat{r} d\hat{\theta} = \hat{Q}_i = \text{constant}. \quad (3)$$

As the pore radius shrinks, the pressure difference needs to increase in order to sustain the flux. We therefore prescribe the pressure at the top and the channel downstream as

$$\hat{p}|_{\hat{z}=0} = \hat{\zeta}(\hat{t}), \quad \hat{p}|_{\hat{z}=1} = 0, \quad (4)$$

where  $\hat{\zeta}(\hat{t})$  is a function, which is monotonically increasing with time  $\hat{t}$ . In addition, the total shear stress  $\hat{\sigma}_s$  at the channel wall, exerted by the nutrient flow, is obtained by

$$\hat{\sigma}_s = \sqrt{|\hat{\boldsymbol{\sigma}} \mathbf{n}|^2 - ((\hat{\boldsymbol{\sigma}} \mathbf{n}) \cdot \mathbf{n})^2}, \quad \hat{\boldsymbol{\sigma}} = \mu \left( \hat{\nabla} \hat{\mathbf{u}} + \hat{\nabla} \hat{\mathbf{u}}^T \right) \Big|_{\hat{r}=\hat{a}}, \quad (5)$$

where  $T$  shows the transpose of the matrix and  $\mathbf{n}$  is the unit vector normal to fluid-cell-layer interface, pointing inwards, given by

$$\mathbf{n} = \frac{\hat{\nabla}(\hat{r} - \hat{a})}{|\hat{\nabla}(\hat{r} - \hat{a})|}. \quad (6)$$

## B. Nutrient concentration

We assume the nutrient is diluted in the fluid flow with concentration  $\hat{c}$ . The rate of change of the nutrient concentration  $\hat{c}$  satisfies

$$\frac{\partial \hat{c}}{\partial \hat{t}} = \hat{\nabla} \cdot \hat{\mathbf{Q}}_n, \quad (7)$$

where

$$\hat{\mathbf{Q}}_n = -\hat{\Xi} \hat{\nabla} \hat{c} + \hat{\mathbf{u}} \hat{c}, \quad (8)$$

is the nutrient flux, with  $\hat{\Xi}$  being the diffusion coefficient of nutrient<sup>29–31</sup>. Nutrient concentration should also satisfy the following boundary conditions<sup>29–31</sup>

$$\begin{aligned} \hat{c}|_{\hat{z}=0} &= \hat{c}_i, \quad \left. \frac{\partial \hat{c}}{\partial \hat{r}} \right|_{\hat{r}=0} = 0, \\ \hat{c}|_{\hat{\theta}=0} &= \hat{c}|_{\hat{\theta}=2\pi}, \quad \left. \frac{\partial \hat{c}}{\partial \hat{\theta}} \right|_{\hat{\theta}=0} = \left. \frac{\partial \hat{c}}{\partial \hat{\theta}} \right|_{\hat{\theta}=2\pi}, \end{aligned} \quad (9)$$

where  $\hat{c}_i$  is the concentration of the nutrient at the pore inlet, pumped into the scaffold. Here we propose that the nutrient consumption happens at the interface where cells interact with nutrient flow, *i.e.* the fluid-cell-layer interface. We further propose that the nutrient consumption is proportional to nutrient concentration, with the coefficient being  $\hat{\eta}$ , which we call the “hunger rate”, or heuristically, how fast the cells consume nutrient<sup>29–31</sup>, that is,

$$\hat{\mathbf{Q}}_n \cdot \mathbf{n} = \hat{\eta} \hat{c}, \quad \text{at } \hat{r} = \hat{a}. \quad (10)$$

## C. Tissue growth

According to the experiments and observational facts<sup>8,32</sup> the cells proliferate more quickly when exposed to more concentrated nutrient solution, higher shear stress at their surface and in regions where the pore configuration has higher curvature<sup>8,33</sup>. Therefore, we propose

$$\frac{\partial \hat{a}}{\partial \hat{t}} = -\hat{\lambda} \hat{c} \hat{\kappa} f(\hat{\sigma}_s). \quad (11)$$

Here,  $\hat{\lambda}$  is the characteristic growth rate ( $\text{mol}^{-1} \text{m}^5 \text{s}^{-1}$ ),  $\hat{\kappa} = \hat{\nabla} \cdot \mathbf{n}$  is the mean curvature and the function  $f$  captures the influence on tissue growth due to the total shear stress  $\hat{\sigma}_s$ , which will be defined later in more detail.

## III. SCALING, NON-DIMENSIONALIZATION

To reduce the number of independent parameters, we nondimensionalize the models for the (i) flow; (ii) nutrient concentration; and (iii) tissue growth described in §II A, §II B and §II C respectively, using appropriate scalings introduced for each one below.

### A. Fluid dynamics

We use the following scalings to nondimensionalize the model given by (1)–(6):

$$\begin{aligned} \hat{\mathbf{u}} &= \frac{\hat{Q}_i}{\pi \hat{R}^2} \mathbf{u} = \frac{\hat{Q}_i}{\pi \hat{R}^2} (\epsilon u, \epsilon v, w), \\ (\hat{p}, \hat{\zeta}, \hat{\sigma}_s) &= \frac{\hat{\mu} \hat{L} \hat{Q}_i}{\pi \hat{R}^4} (p, \zeta, \sigma_s), \\ (\hat{r}, \hat{a}, \hat{z}) &= \hat{L} (\epsilon r, \epsilon a, z), \end{aligned} \quad (12)$$

where  $\mu$  is the viscosity and  $\hat{Q}_i$  is the inlet flux.  $\hat{L}$  and  $\hat{R}$  are the length and the typical pore radius, respectively.  $u, v, w, p, \zeta, \sigma_s, r, a$  and  $z$ , are the corresponding dimensionless variables. From (1), the corresponding dimensionless equations governing the flow are given by

$$\frac{1}{\epsilon^2} \frac{\partial p}{\partial r} = \frac{1}{r} \frac{\partial}{\partial r} \left( r \frac{\partial u}{\partial r} \right) + \frac{1}{r^2} \frac{\partial^2 u}{\partial \theta^2} + \epsilon^2 \frac{\partial^2 u}{\partial z^2} - \frac{u}{r^2} - \frac{2}{r^2} \frac{\partial v}{\partial \theta}, \quad (13)$$

$$\frac{1}{\epsilon^2 r} \frac{\partial p}{\partial \theta} = \frac{1}{r} \frac{\partial}{\partial r} \left( r \frac{\partial v}{\partial r} \right) + \frac{1}{r^2} \frac{\partial^2 v}{\partial \theta^2} + \epsilon^2 \frac{\partial^2 v}{\partial z^2} - \frac{v}{r^2} + \frac{2}{r^2} \frac{\partial u}{\partial \theta}, \quad (14)$$

$$\frac{\partial p}{\partial z} = \frac{1}{r} \frac{\partial}{\partial r} \left( r \frac{\partial w}{\partial r} \right) + \frac{1}{r^2} \frac{\partial^2 w}{\partial \theta^2} + \epsilon^2 \frac{\partial^2 w}{\partial z^2}, \quad (15)$$

$$\frac{1}{r} \frac{\partial}{\partial r} (ru) + \frac{1}{r} \frac{\partial v}{\partial \theta} + \frac{\partial w}{\partial z} = 0. \quad (16)$$

Substituting (12) into the dimensional boundary conditions (2) yields the dimensionless boundary conditions

$$\begin{aligned} u = v = w = 0 & \quad \text{on} \quad r = a(\theta, z, t), \\ u = v = \frac{\partial w}{\partial r} = 0 & \quad \text{at} \quad r = 0. \end{aligned} \quad (17)$$

The dimensionless form of the constant fluid influx condition (3), is

$$\int_0^{2\pi} \int_0^a \sqrt{\epsilon^2 u^2 + \epsilon^2 v^2 + w^2} r dr d\theta = \pi. \quad (18)$$

Corresponding to (4), we assume that the dimensionless pressure drop across the length of the pore is given by  $\zeta(t)$  ( $t$  is the dimensionless time and the scale will be introduced later in §III C), a function monotonically increasing in  $t$  to keep the flux constant, as the pore shrinks due to cell proliferation. We therefore complete the system by applying the dimensionless boundary conditions

$$p|_{z=0} = \zeta(t), \quad p|_{z=1} = 0. \quad (19)$$

The dimensionless total shear stress at the channel walls, exerted by the nutrient flow, after manipulating (5), is given by

$$\sigma_s = \sqrt{|\boldsymbol{\sigma n}|^2 - ((\boldsymbol{\sigma n}) \cdot \mathbf{n})^2}, \quad \boldsymbol{\sigma} = \begin{pmatrix} 2\epsilon \frac{\partial u}{\partial r} & \epsilon \left( \frac{1}{r} \frac{\partial u}{\partial \theta} - \frac{v}{r} + \frac{\partial v}{\partial r} \right) & \epsilon^2 \frac{\partial u}{\partial z} + \frac{\partial w}{\partial r} \\ \epsilon \left( \frac{1}{r} \frac{\partial u}{\partial \theta} - \frac{v}{r} + \frac{\partial v}{\partial r} \right) & 2\epsilon \left( \frac{1}{r} \frac{\partial v}{\partial \theta} + \frac{u}{r} \right) & \epsilon^2 \frac{\partial v}{\partial z} + \frac{1}{r} \frac{\partial w}{\partial \theta} \\ \epsilon^2 \frac{\partial u}{\partial z} + \frac{\partial w}{\partial r} & \epsilon^2 \frac{\partial v}{\partial z} + \frac{1}{r} \frac{\partial w}{\partial \theta} & 2\epsilon \frac{\partial w}{\partial z} \end{pmatrix}, \quad (20)$$

where the unit normal vector to the fluid-cell-layer interface, pointing inwards (6), is simplified as

$$\mathbf{n} = \frac{\left( \mathbf{e}_r - \frac{1}{r} \frac{\partial a}{\partial \theta} \mathbf{e}_\theta - \epsilon \frac{\partial a}{\partial z} \mathbf{e}_z \right)}{\sqrt{1 + \frac{1}{r^2} \left( \frac{\partial a}{\partial \theta} \right)^2 + \epsilon^2 \left( \frac{\partial a}{\partial z} \right)^2}}. \quad (21)$$

## B. Nutrient concentration

In order to nondimensionalize the model (7)–(10) presented in §II B, we use (12) along with a new scaling for the nutrient concentration

$$\hat{c} = \hat{c}_i c, \quad (22)$$

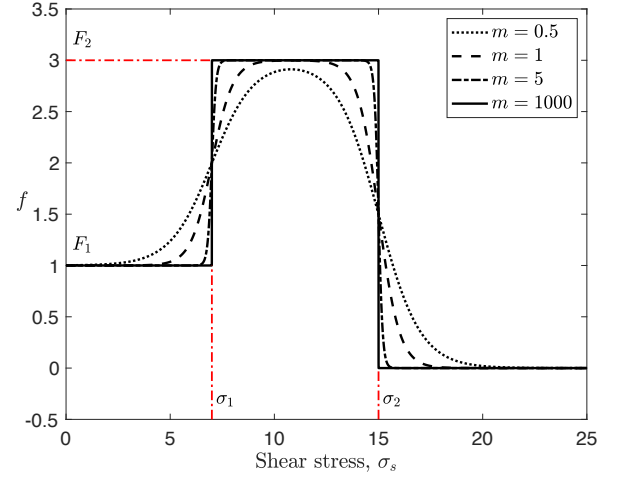


FIG. 2. The growth function  $f$  that appears in (27) and (28), with  $F_1 = 1$ ,  $F_2 = 3$ ,  $\sigma_1 = 7$ , and  $\sigma_2 = 15$  for several values of  $m$ .

to arrive at

$$\frac{1}{\epsilon \text{Pe}} \left[ \frac{1}{r} \frac{\partial}{\partial r} \left( r \frac{\partial c}{\partial r} \right) + \frac{1}{r^2} \frac{\partial^2 c}{\partial \theta^2} + \epsilon^2 \frac{\partial^2 c}{\partial z^2} \right] = \frac{\partial c}{\partial r} u + \frac{1}{r} \frac{\partial c}{\partial \theta} v + \frac{\partial c}{\partial z} w, \quad \text{Pe} = \frac{\epsilon \hat{L} \hat{Q}_i}{\pi \hat{R}^2 \hat{\Xi}}, \quad (23)$$

$$c|_{z=0} = 1, \quad \frac{\partial c}{\partial r} \Big|_{r=0} = 0, \quad (24)$$

$$c|_{\theta=0} = c|_{\theta=2\pi}, \quad \frac{\partial c}{\partial \theta} \Big|_{\theta=0} = \frac{\partial c}{\partial \theta} \Big|_{\theta=2\pi},$$

$$\frac{1}{\epsilon \text{Pe}} \left( \frac{\partial c}{\partial r}, \frac{1}{r} \frac{\partial c}{\partial \theta}, \epsilon \frac{\partial c}{\partial z} \right) \cdot \mathbf{n} = -\eta c, \quad \text{at} \quad r = a, \quad (25)$$

$$\eta = \frac{\pi \hat{R}^2 \hat{\eta}}{\epsilon \hat{Q}_i},$$

where  $\text{Pe}$  and  $\eta$  are the Péclet number associated with the ratio of advective to diffusive transport rates of nutrients, and the dimensionless hunger rate, respectively. Note that, the time scale of cell proliferation, is much longer compared to that of nutrient flow transport<sup>8,14</sup>, therefore, we employ the quasi-static assumption for (7) to obtain (23).

## C. Tissue growth

Using the scalings given in (12) and (22) along with the additional scales

$$\hat{t} = \frac{\hat{R}^2}{\lambda \hat{c}_i} t, \quad \hat{\kappa} = \frac{1}{\hat{R}} \kappa, \quad (26)$$

for the time and curvature, respectively, we can simplify (11) and find the dimensionless growth law as

$$\frac{\partial a}{\partial t} = -c \kappa f(\sigma_s). \quad (27)$$

Experimental data and analytical references<sup>8,14</sup> reveal that the functional form of  $f$ , introduced first in (11), can be interpreted as a piece-wise constant function as shown in Fig. 2, which has a general form of

$$f(x) = F_1 + (F_2 - F_1) \left[ \frac{1 + \tanh(m(x - \sigma_1))}{2} \right] - F_2 \left[ \frac{1 + \tanh(m(x - \sigma_2))}{2} \right]. \quad (28)$$

Here  $F_1 < F_2$ ,  $\sigma_1 < \sigma_2$ ,  $m \gg 1$  and based on the shear-stress scaling in (12),  $\sigma_1$  and  $\sigma_2$  will typically be order-one quantities<sup>8,14</sup>. For large values of  $m$ , this corresponds to a function that has three regions in which it is approximately constant, connected by rapid but smooth transition regions<sup>8,14,25</sup>. According to (28) as well as Fig. 2, the tissue growth is low, enhanced and zero when the total shear stress at the channel walls, exerted by the nutrient flow, is low, moderate and high, respectively.

#### IV. ASYMPTOTIC ANALYSIS

The complete dimensionless system described in §III is extremely hard to solve analytically, and it is also computationally costly to solve numerically in a brute force way. Therefore, we make use of the fact that the pore aspect ratio  $\epsilon = \hat{R}/\hat{L} \ll 1$ . This allows us to achieve a simpler, computationally-feasible, reduced asymptotic model. As stated earlier, we assume the initial fluid-cell-layer interface is sufficiently thin, so that it can be approximated by the underlying substrate geometry. Since the substrate is assumed to be roughly circular with small azimuthal and axial variation, we implement the relegation of spatial variations to first (axial) and second (azimuthal and axial) order in the aspect ratio  $\epsilon$ .

We assume that the fluid-cell-layer interface is expressed as

$$a(\theta, z, t) = a_0(t) + \epsilon a_1(z, t) + \epsilon^2 a_2(\theta, z, t) + \mathcal{O}(\epsilon^3), \quad (29)$$

where

$$a_2(\theta, z, t) = \Lambda_2(z, t) \cos(n\theta) + \Upsilon_2(z, t), \quad (30)$$

$\Lambda_2(z, t)$  and  $\Upsilon_2(z, t)$  are functions to be pinned down and  $n$  is an integer that describes the number of lobes in the geometry of the underlying substrate<sup>14</sup>. Although the above assumption poses constraints on the class of pores we can study, it is essential in attaining a balance between some level of generality and feasible asymptotic calculations. Here the initial configuration of the fluid-cell-layer interface  $a(\theta, z, 0)$  is given by the shape of the underlying substrate, and its subsequent evolution is described by the equation of cell growth (27). Below, we asymptotically expand the variables  $u$ ,  $v$ ,  $w$ ,  $p$ ,  $\zeta$ ,  $c$ ,  $\sigma_s$ ,  $f$  and  $\kappa$  in the form of

$$x = x_0 + \epsilon x_1 + \epsilon^2 x_2 + \mathcal{O}(\epsilon^3), \quad (31)$$

where  $x$  is any variable listed above. With (29), the unit vector normal to fluid-cell-layer interface, pointing inwards (21) simplifies to

$$\mathbf{n} = \left( \mathbf{e}_r - \epsilon^2 \frac{1}{r} \frac{\partial a_2}{\partial \theta} \mathbf{e}_\theta - \epsilon^2 \frac{\partial a_1}{\partial z} \mathbf{e}_z \right) \Big|_{r=a_0} + \mathcal{O}(\epsilon^3). \quad (32)$$

#### A. Fluid dynamics

Assuming that the flow is independent of  $\theta$  to leading order in  $\epsilon$ , (13)–(20) along with the asymptotic expansions (31) yield the leading-order velocities  $u_0$ ,  $v_0$ ,  $w_0$ , pressure  $p_0$  and pressure at the pore inlet  $\zeta_0$ . Therefore, at  $\mathcal{O}(1)$

$$\begin{aligned} u_0 &= 0, & v_0 &= 0, & w_0 &= \frac{\zeta_0}{4} (a_0^2 - r^2), \\ p_0 &= \zeta_0(1 - z), & \zeta_0 &= \frac{8}{a_0^4}. \end{aligned} \quad (33)$$

Similarly, for  $\mathcal{O}(\epsilon)$ , we obtain

$$\begin{aligned} u_1 &= \frac{\partial a_1}{\partial z} \frac{\zeta_0}{4a_0} r (a_0^2 - r^2), & v_1 &= 0, \\ w_1 &= \frac{a_1 \zeta_0}{2a_0} (2r^2 - a_0^2), \end{aligned} \quad (34)$$

$$p_1 = -\frac{4\zeta_0}{a_0} \int_z^1 a_1(z', t) dz', \quad \zeta_1 = -\frac{4\zeta_0}{a_0} \int_0^1 a_1(z, t) dz. \quad (35)$$

Finally for  $\mathcal{O}(\epsilon^2)$

$$w_2 = \left[ \frac{\Lambda_2}{2} a_0^{1-n} r^n \cos n\theta + \tilde{w}_2(r, z, t) \right] \zeta_0, \quad (36)$$

$$\begin{aligned} \frac{a_0^4}{4} p_2 &= \left[ 3a_0^2 \int_z^1 a_1^2(z', t) dz' - a_0^3 \int_z^1 \Upsilon_2(z', t) dz' \right. \\ &\quad \left. + \frac{1}{4} \int_z^1 a_1^4(z', t) dz' \right] \zeta_0, \end{aligned} \quad (37)$$

$$\begin{aligned} \zeta_2 &= \frac{4}{a_0^4} \left[ 3a_0^2 \int_0^1 a_1^2(z', t) dz' - a_0^3 \int_0^1 \Upsilon_2(z', t) dz' \right. \\ &\quad \left. + \frac{1}{4} \int_0^1 a_1^4(z', t) dz' \right] \zeta_0, \end{aligned} \quad (38)$$

$$\begin{aligned} w_2 &= \left[ \frac{\Lambda_2}{2} a_0^{1-n} r^n \cos n\theta + \frac{1}{a_0^4} \left( -3a_0^2 a_1^2 + a_0^3 \Upsilon_2 - \frac{a_1^4}{4} \right) \right. \\ &\quad \left. (r^2 - a_0^2) - \frac{7}{4} a_1^2 + \frac{a_0 \Upsilon_2}{2} \right] \zeta_0. \end{aligned} \quad (39)$$

In addition, the dimensionless shear stress at the fluid-cell-layer interface is

$$\sigma_s = \sigma_{s_0} + \epsilon \sigma_{s_1} + \epsilon^2 (\sigma_{s_{2a}} \cos n\theta + \sigma_{s_{2b}}) + \mathcal{O}(\epsilon^3), \quad (40)$$

where,

$$\begin{aligned} \sigma_{s_0} &= \frac{a_0}{2} \zeta_0, \quad \sigma_{s_1} = 2a_1 \zeta_0, \\ \sigma_{s_{2a}} &= \frac{n\Lambda_2 \zeta_0}{2}, \quad \sigma_{s_{2b}} = \frac{1}{a_0^3} (-6a_0^2 a_1^2 + 2a_0^3 \Upsilon_2 - \frac{a_1^4}{2}) \zeta_0. \end{aligned} \quad (41)$$

Furthermore, the dimensionless curvature  $\kappa$  can be found as

$$\begin{aligned} \kappa &= \kappa_0(t) + \epsilon^2 \kappa_2(z, t) \cos n\theta + \mathcal{O}(\epsilon^3), \\ \kappa_0 &= \frac{1}{a_0}, \quad \kappa_2 = \frac{n^2 \Lambda_2}{a_0^2}. \end{aligned} \quad (42)$$

## B. Nutrient concentration

We substitute the asymptotic expansions (31) into (23)–(25) to retain the nutrient concentration at  $\mathcal{O}(1)$ ,  $\mathcal{O}(\epsilon)$  and  $\mathcal{O}(\epsilon^2)$ . Note that, Péclet number is defined as the ratio of advective to diffusive transport rates of nutrients. Here we consider a distinguished limit of the nutrient Péclet number, which is  $\text{Pe} = \mathcal{O}(1)$ . One may consider  $\text{Pe} = \mathcal{O}(\epsilon)$ , if the main interest is on the effects of axial diffusion of the nutrient<sup>29–31</sup>. Our model can be readily extended to the general scenario. The dimensionless nutrient concentration (23) at  $\mathcal{O}(\frac{1}{\epsilon})$ ,  $\mathcal{O}(1)$ ,  $\mathcal{O}(\epsilon)$  and  $\mathcal{O}(\epsilon^2)$  respectively, simplify to

$$\frac{1}{\text{Pe}} \left[ \frac{1}{r} \frac{\partial}{\partial r} \left( r \frac{\partial c_0}{\partial r} \right) + \frac{1}{r^2} \frac{\partial^2 c_0}{\partial \theta^2} \right] = 0, \quad (43)$$

$$\frac{1}{\text{Pe}} \left[ \frac{1}{r} \frac{\partial}{\partial r} \left( r \frac{\partial c_1}{\partial r} \right) + \frac{1}{r^2} \frac{\partial^2 c_1}{\partial \theta^2} \right] = \frac{\partial c_0}{\partial r} u_0 + \frac{1}{r} \frac{\partial c_0}{\partial \theta} v_0 + \frac{\partial c_0}{\partial z} w_0, \quad (44)$$

$$\begin{aligned} \frac{1}{\text{Pe}} \left[ \frac{1}{r} \frac{\partial}{\partial r} \left( r \frac{\partial c_2}{\partial r} \right) + \frac{1}{r^2} \frac{\partial^2 c_2}{\partial \theta^2} + \frac{\partial^2 c_0}{\partial z^2} \right] = \\ \frac{\partial c_0}{\partial r} u_1 + \frac{\partial c_1}{\partial r} u_0 + \frac{1}{r} \frac{\partial c_0}{\partial \theta} v_1 + \frac{1}{r} \frac{\partial c_1}{\partial \theta} v_0 + \frac{\partial c_0}{\partial z} w_1 + \frac{\partial c_1}{\partial z} w_0, \end{aligned} \quad (45)$$

$$\begin{aligned} \frac{1}{\text{Pe}} \left[ \frac{1}{r} \frac{\partial}{\partial r} \left( r \frac{\partial c_3}{\partial r} \right) + \frac{1}{r^2} \frac{\partial^2 c_3}{\partial \theta^2} + \frac{\partial^2 c_1}{\partial z^2} \right] = \\ \frac{\partial c_0}{\partial r} u_2 + \frac{\partial c_1}{\partial r} u_1 + \frac{\partial c_2}{\partial r} u_0 + \frac{1}{r} \frac{\partial c_0}{\partial \theta} v_2 + \frac{1}{r} \frac{\partial c_1}{\partial \theta} v_1 \\ + \frac{1}{r} \frac{\partial c_2}{\partial \theta} v_0 + \frac{\partial c_0}{\partial z} w_2 + \frac{\partial c_1}{\partial z} w_1 + \frac{\partial c_2}{\partial z} w_0. \end{aligned} \quad (46)$$

The corresponding dimensionless boundary conditions given in (25) simplify to

$$\frac{1}{\text{Pe}} \frac{\partial c_0}{\partial r} = 0, \quad \text{at } r = a_0, \quad (47)$$

$$\frac{1}{\text{Pe}} \frac{\partial c_1}{\partial r} = -\eta c_0, \quad \text{at } r = a_0, \quad (48)$$

$$\frac{1}{\text{Pe}} \left( \frac{\partial c_2}{\partial r} - \frac{1}{r^2} \frac{\partial a_2}{\partial \theta} \frac{\partial c_0}{\partial \theta} \right) = -\eta c_1, \quad \text{at } r = a_0, \quad (49)$$

$$\frac{1}{\text{Pe}} \left( \frac{\partial c_3}{\partial r} - \frac{1}{r^2} \frac{\partial a_2}{\partial \theta} \frac{\partial c_1}{\partial \theta} - \frac{\partial a_1}{\partial z} \frac{\partial c_0}{\partial z} \right) = -\eta c_2, \quad \text{at } r = a_0, \quad (50)$$

by using (32).

### 1. Leading order analysis

From (43) and (47) we obtain  $\frac{\partial c_0}{\partial r} = 0$ , hence  $c_0$  is a function of  $z$  only. Using (33) in (44) yields

$$\frac{1}{\text{Pe}} \left[ \frac{1}{r} \frac{\partial}{\partial r} \left( r \frac{\partial c_1}{\partial r} \right) + \frac{1}{r^2} \frac{\partial^2 c_1}{\partial \theta^2} \right] = \frac{\partial c_0}{\partial z} \frac{\zeta_0}{4} (a_0^2 - r^2). \quad (51)$$

Next, we integrate (51) over the pore cross section by applying  $\int_0^{2\pi} \int_0^{a_0} \cdot r dr d\theta$  operator, along with (24), to obtain

$$\frac{\partial c_0}{\partial z} = -2\eta a_0 c_0, \quad (52)$$

and together with the condition that  $c_0|_{z=0} = 1$  (see (24)), we arrive at

$$c_0(z) = e^{-2\eta a_0 z}. \quad (53)$$

### 2. First order analysis

We use (33), (34) and (53) to simplify (45) and then integrate over the pore cross section and apply (24), to obtain

$$\frac{1}{\text{Pe}} \left[ a_0 \frac{\partial c_2}{\partial r} \Big|_{r=a_0} + \frac{1}{2} a_0^2 \frac{\partial^2 c_0}{\partial z^2} \right] = \frac{\zeta_0 a_0^4}{16} \frac{\partial c_1}{\partial z}. \quad (54)$$

Simplifying (49) by (53) and then plug in to (54) gives

$$\frac{\partial c_1}{\partial z} + 2a_0 \eta c_1 = \frac{4a_0^4}{\text{Pe}} \eta^2 e^{-2\eta a_0 z}, \quad (55)$$

which is solved (by using the initial condition  $c_1|_{z=0} = 0$  given in (24)),

$$c_1(z) = \frac{4a_0^4}{\text{Pe}} \eta^2 z e^{-2a_0 \eta z}. \quad (56)$$

### 3. Second order analysis

Similarly, we plug in (33), (34) and (39) into (46) and (50) to obtain

$$\frac{1}{\text{Pe}} \left[ a_0 \frac{\partial c_3}{\partial r} \Big|_{r=a_0} + \frac{1}{2} a_0^2 \frac{\partial^2 c_1}{\partial z^2} \right] = \frac{\zeta_0 (-2a_0^2 a_1^2 + a_1^4)}{16} \frac{\partial c_0}{\partial z} + \frac{\zeta_0 a_0^4}{16} \frac{\partial c_2}{\partial z}, \quad (57)$$

$$\frac{1}{\text{Pe}} \frac{\partial c_3}{\partial r} \Big|_{r=a_0} - \frac{1}{\text{Pe}} \frac{\partial a_1}{\partial z} \frac{\partial c_0}{\partial z} = -\eta c_2. \quad (58)$$

Combining (57) and (58), with some manipulations and using (53), (56) and  $c_2|_{z=0} = 0$  (see (24)), gives

$$c_2(z) = e^{-2a_0\eta z} \left[ -\frac{4\eta a_0^2(a_1 - a_1|_{z=0})}{\text{Pe}} - \frac{16a_0^7\eta^3}{\text{Pe}^2} z + \frac{8a_0^8\eta^4}{\text{Pe}^2} z^2 - 2\eta \int_0^z \left( \frac{2a_1^2}{a_0} - \frac{a_1^4}{a_0^3} \right) dz' \right]. \quad (59)$$

### C. Tissue growth

We simplify (27) by (29), (41) and (42) along with Taylor expansion of  $f$  (given in (28)) to obtain

$$\frac{\partial a_0}{\partial t} = -c_0 \kappa_0 f, \quad (60)$$

$$\frac{\partial a_1}{\partial t} = -c_0 \kappa_0 \sigma_{s_1} f' - c_1 \kappa_0 f, \quad (61)$$

$$\frac{\partial \Lambda_2}{\partial t} = -c_0 \kappa_2 f - c_0 \kappa_0 \sigma_{s_{2a}} f', \quad (62)$$

$$\frac{\partial \Upsilon_2}{\partial t} = -c_2 \kappa_0 f - c_1 \kappa_0 \sigma_{s_1} f' - c_0 \kappa_0 (\sigma_{s_{2b}} f' + \frac{1}{2} \sigma_{s_1}^2 f''). \quad (63)$$

Here  $f, f', f''$  are all evaluated at  $\sigma_{s_0}$  and the initial values for  $a_0, a_1, \Lambda_2$  and  $\Upsilon_2$  are prescribed. Note that,  $f, \kappa_0, \kappa_2, c_0, c_1$  and  $c_2$  are given in (28), (42), (53), (56) and (59), respectively.

## V. RESULTS

In this section, we present and analyze simulations of the models (28), (42), (53), (56), (59), (60)-(63). Our numerical scheme is straightforward, based on implicit time-stepping of fluid-cell-layer interface evolution (i.e., (60)-(63)), and trapezoidal quadrature to evaluate the integrals in (59). To fully specify our model, various dimensional and dimensionless parameters given in Tables I and II, respectively, are estimated based on the typical ranges arising in tissue engineering applications<sup>8,14,31,34-36</sup>. Specifically, the dimensionless parameter Péclet number  $\text{Pe}$  and hunger rate  $\eta$ , which show the ratio of advective to diffusive transport rates of nutrients and how fast the cells consume the nutrients, respectively. Their values vary for different nutrients and cells respectively, and  $\text{Pe} = 1$ ,  $\eta = 0 - 0.1$  and  $\epsilon = 0.2$  are chosen in all simulations (see Table II).

### A. Incubation simulation

Figures 3 and 4 show the shape of the fluid-cell-layer interface at different times for several values of hunger rate  $\eta = 0, 0.05$  and  $0.1$  in (a), (b) and (c), respectively (see Figs. 3(d) and 4(d) (Multimedia view)). In Fig. 3, the initial geometry of the pore is wider on the top and narrower at the bottom with  $a_1(z, 0) = -z - 0.5$ , while in Fig. 4 is the opposite and  $a_1(z, 0) = z - 0.5$ . In both figures  $a_0(0) = 0.9$ ,  $\Lambda_2(z, 0) = -z + 2$ ,  $\Upsilon_2(z, 0) = -z + 2$  and  $n = 4$ . At  $t = 0$ , when the pore is at its initial configuration, cells with negligible thickness are attached to the pore wall, therefore,  $a(\theta, z, t)$  should be regarded as the initial shape of the pore. As nutrient passes through the pore, cells consume the nutrients and proliferate, gradually filling the space within the pore, which can be observed from the shrinkage of fluid-cell-layer as time passes ( $a(\theta, z, t)$  is decreasing in  $t$ ). This can be seen as the fluid-cell-layer shrinks more as time passes. Dimensionless final time  $t_f = 0.25$  is chosen to be sufficiently large so that the incubation has terminated under all the cases shown in the figures.

Another important observation is the “sequential eating” phenomena of cells in the pore. Our results show that the larger hunger rate is, the longer time it takes for the incubation process to terminate. This can be explained as below. Given a fixed nutrient supply, when hunger rate is large, initially a larger portion of the nutrient is consumed by cells at the top, so very few is left for cells at the bottom. Recall that cells at the top of the pore stop to proliferate as the shear stress increases beyond its threshold  $\sigma_2$  (see (27) and (28)). As consumption by cells at the top decreases, more nutrient is left for cells at the bottom. This demonstrates the “sequential eating” phenomena, which also appears in experimental observations<sup>19</sup>. On the other hand, when  $\eta = 0$ , concentration is held constant across the pore, so cells at different depths of the pore are exposed to the same amount of nutrient. Thus, cells will proliferate simultaneously. The larger the hunger rate, the more the “sequential eating” phenomena will be, and therefore it takes longer for the system to terminate and reaches the steady state (no proliferation happens). Such observations can be more vividly seen in Figs. 3(d) and 4(d) (Multimedia view).

Figures 5(a) and (b) show the cross section of scaffold pore at the initial and final ( $t_f$ ) times of the tissue growth process respectively, for two values of hunger rate  $\eta = 0$  and  $0.1$  with the initial pore radius as in Fig. 3. As observed, the tissue will grow so that ultimately the tube is circular in cross section, but the radius may vary along the axis, depending on the initial tube geometry and the hunger rate. Figures 5(c)-(f) compares the radii of the fluid-cell-layer interface of the model we propose in this paper with those of the model developed in Sanaei et al.<sup>14</sup> (see  $\eta = 0$  curves). The leading order of the radius of the fluid-cell-layer interface  $a_0$  varies at different  $z$  level when  $\eta = 0.1$ , but with  $\eta = 0$ ,  $a_0$  is of the same value throughout the scaffold pore. This is also observed

Parameter	Description	Typical value
$\bar{Q}_i$	Inlet flux	1 $\mu\text{l}/\text{min}$
$\bar{R}$	Fluid-cell-layer interface radius	400 $\mu\text{m}$
$\bar{L}$	Fluid-cell-layer interface length	2 mm
$\bar{c}_i$	Nutrient concentration at the pore inlet	1-10 mol/m <sup>3</sup>
$\bar{\Xi}$	Diffusion coefficient of nutrient	10 <sup>-8</sup> – 10 <sup>-6</sup> m <sup>2</sup> /s
$\bar{\eta}$	Hunger rate	0 – 10 <sup>-4</sup> m/s

TABLE I. Dimensional parameter values<sup>8,14,31,34–36</sup> for the model.

Parameter	Formula	Typical value
$\epsilon$	$\bar{R}/\bar{L}$	0.2
Pe	$(\epsilon\bar{L}\bar{Q}_i)/(\pi\bar{R}^2\bar{\Xi})$	1 – 10
$\eta$	$(\pi\bar{R}^2\bar{\eta})/(\epsilon\bar{Q}_i)$	0 – 0.25

TABLE II. Dimensionless parameters values<sup>8,14,31,34–36</sup> for the model.

in  $a_1$  and  $\Upsilon_2$ . The difference in radii with respect to  $z$  for a non-zero value of  $\eta$ , causes the difference in shear stress and as a consequence affects the amount of tissue growth in the tube. On the other hand,  $\Lambda_2$  varies along the tube axis for both hunger rate values. Fig. 5(g) and (h) show that the leading order of the shear stress  $\sigma_{s_0}$  varies with  $z$ , when  $\eta = 0.1$  and the first order of the shear stress  $\sigma_{s_1}$  takes longer time to reach the steady state compared to the scenario when  $\eta = 0$ . One can easily check that, for other initial conditions prescribed in Sanaei et al.<sup>14</sup>, our model yields the same results when hunger rate  $\eta$  is set to be zero, which is equivalent to assuming that no nutrient depletion happens in the model. Hence, our model is compatible with the models proposed in previous literature<sup>14,25,33</sup>, and provides more insights of the reality when nutrient concentration is not constant throughout the scaffold pores.

## B. Nutrient consumption and “hunger rate”

There are several noticeable differences when the nutrient concentration depletion is added into consideration. As mentioned before,  $\eta = 0$  corresponds to the assumption that nutrient supply is in excess, so nutrient concentration is held at constant across the pore axis. As expected,  $a_0$  is uniform at different height of the pore (see Fig. 5(c), the black curves at different height collapse to the red curve at  $z = 0$ ). The red curves in Fig. 5(b) show that when nutrient consumption is considered,  $a$  is smaller for larger values of  $z$ , indicating that there is more tissue growth at the bottom part of the pore. This can be explained by the fact that the shear stress dominant term  $\sigma_{s_0}$  in Fig. 5(g) grows slower when  $\eta = 0.1$  compared to  $\eta = 0$ . As a result, the shear stress would increase slower in the former case, and due to the bell

shape of  $f$  (see Fig. 2), cells in the former case will experience longer period of growth, which can be seen in Fig. 5(c) (takes longer time for  $a_0$  to reach the steady state phase). In addition, the curves for  $\sigma_{s_1}$  with  $\eta = 0.1$  in Fig. 5(h) also reveal a delayed change compared to the case when  $\eta = 0$ .

Evidently, the most dominant consequence of cells’ nutrient consumption is the change in the nutrient concentration across the pore. In Fig. 6, we compare the nutrient concentration  $c = c_0 + \epsilon c_1 + \epsilon^2 c_2 + \mathcal{O}(\epsilon^3)$  (see (53), (56) and (59) for  $c_0$ ,  $c_1$  and  $c_2$ , respectively) for two choices of two hunger rates,  $\eta = 0.05$  and 0.10. Figures 6(a) and (b) show that, regardless of time  $t$  and depth  $z$  chosen, the concentration associated with the case  $\eta = 0.05$  is always larger than that associated with  $\eta = 0.10$ . This can be primarily attributed to the leading term of concentration  $c_0$ . In Figs. 6(c) and (d), we observe that throughout the entire simulation,  $c_0$  and  $c_1$  are lower when  $\eta$  is higher, regardless of time  $t$  and depth  $z$ . More drastic variation is observed in higher order terms of nutrient concentration  $c$  when hunger rate  $\eta$  is larger in Figs. 6(e)-(h). Nevertheless, dynamics in concentration  $c$  is mostly captured by the leading term  $c_0$ . Hence, it can be concluded that cells with larger “hunger rate”  $\eta$  tend to “eat more”, resulting a lower nutrient concentration in the pore.

Besides consuming more nutrient, cells with larger  $\eta$  also “eat faster.” In Fig. 6(b), the concentration  $c$  associated with  $\eta = 0.10$  decreases more rapidly with respect to  $z$  compared to the case when  $\eta = 0.05$ . Since the nutrient flows into the pore from  $z = 0$ , it illustrates that the consumption of nutrient by cells residing on the top part of the pore leads to an obvious decrease of nutrient concentration there. As the time goes, however, nutrient concentration decreases less rapidly. The intuition is that the cells residing on the top part in the scaffold have stopped growing, therefore they do not consume the nutrient anymore. They take the “best” position to consume the nutrient, so they grow quickly and the radii of fluid-cell-layer have shrunk small enough so that the shear stress  $\sigma_{s_0} > \sigma_2$ . Then according to (27) and (28) the proliferation stops. At a specific depth  $z_0$ , as cells above gradually stop growing, less nutrient is being consumed and hence concentration at this depth  $c(z = z_0, t)$  is increasing with respect to  $t$ . Finally when all cells above  $z_0$  stop growing,  $c(z = z_0, t)$  becomes constant, as is evident in Fig. 7. The timing that cells above



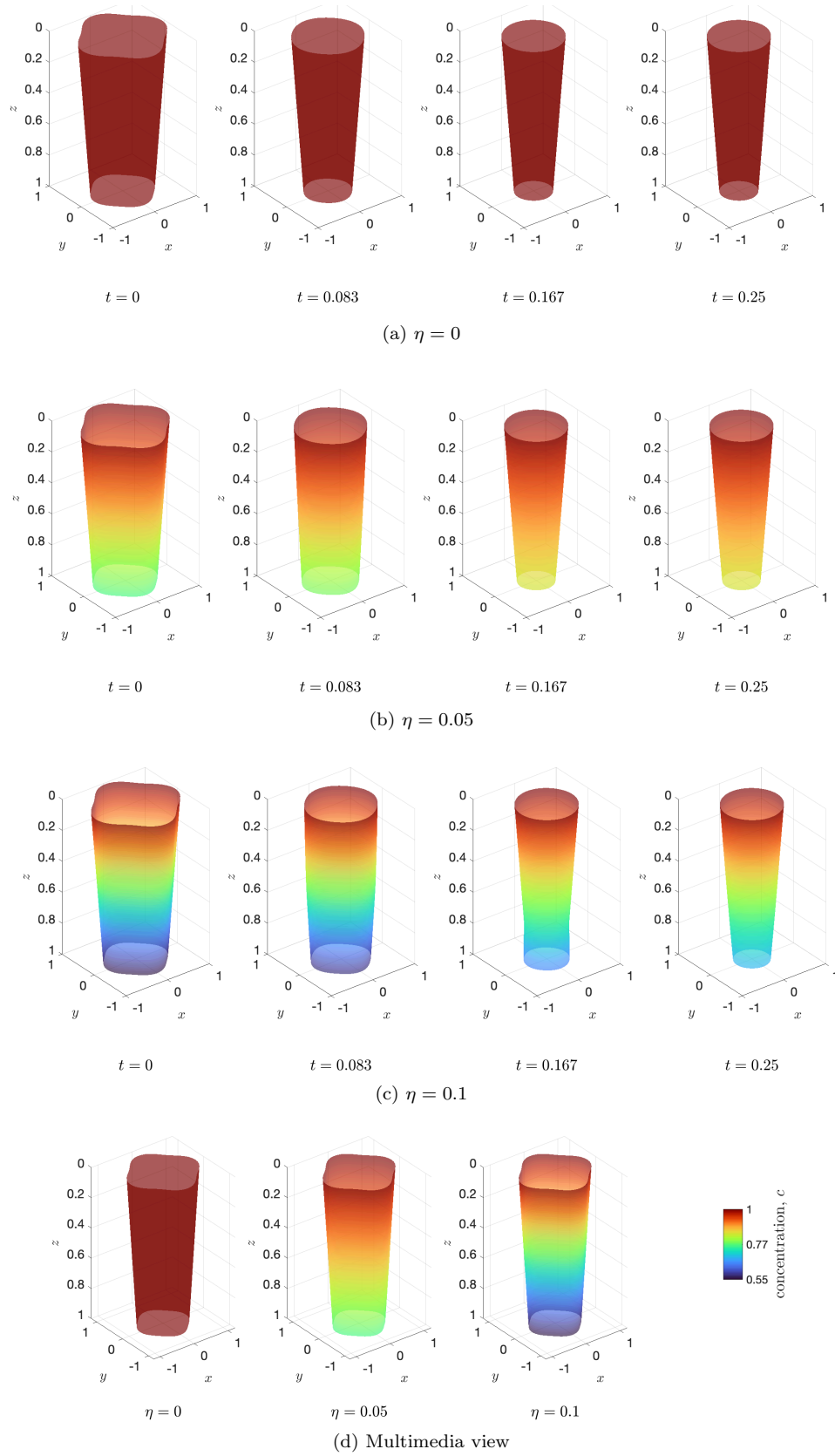


FIG. 3. (a)-(c) show the fluid-cell-layer interface  $a(\theta, z, t) = a_0(t) + \epsilon a_1(z, t) + \epsilon^2 (\Lambda_2(z, t) \cos(n\theta) + \Upsilon_2(z, t)) + O(\epsilon^3)$ , at different times with hunger rates  $\eta = 0, 0.05$  and  $0.1$ , respectively. Here,  $a_0(0) = 0.9$ ,  $a_1(z, 0) = -z - 0.5$ ,  $\Lambda_2(z, 0) = -z + 2$ ,  $\Upsilon_2(z, 0) = -z + 2$ ,  $n = 4$ ,  $\epsilon = 0.2$  and  $\text{Pe} = 1$ .  $f$  is defined and graphed in (28) and Fig. 2 respectively, with  $m \rightarrow \infty$ . The colorbar shows the nutrient concentration. (d) provides more details on the pore evolution (Multimedia view).

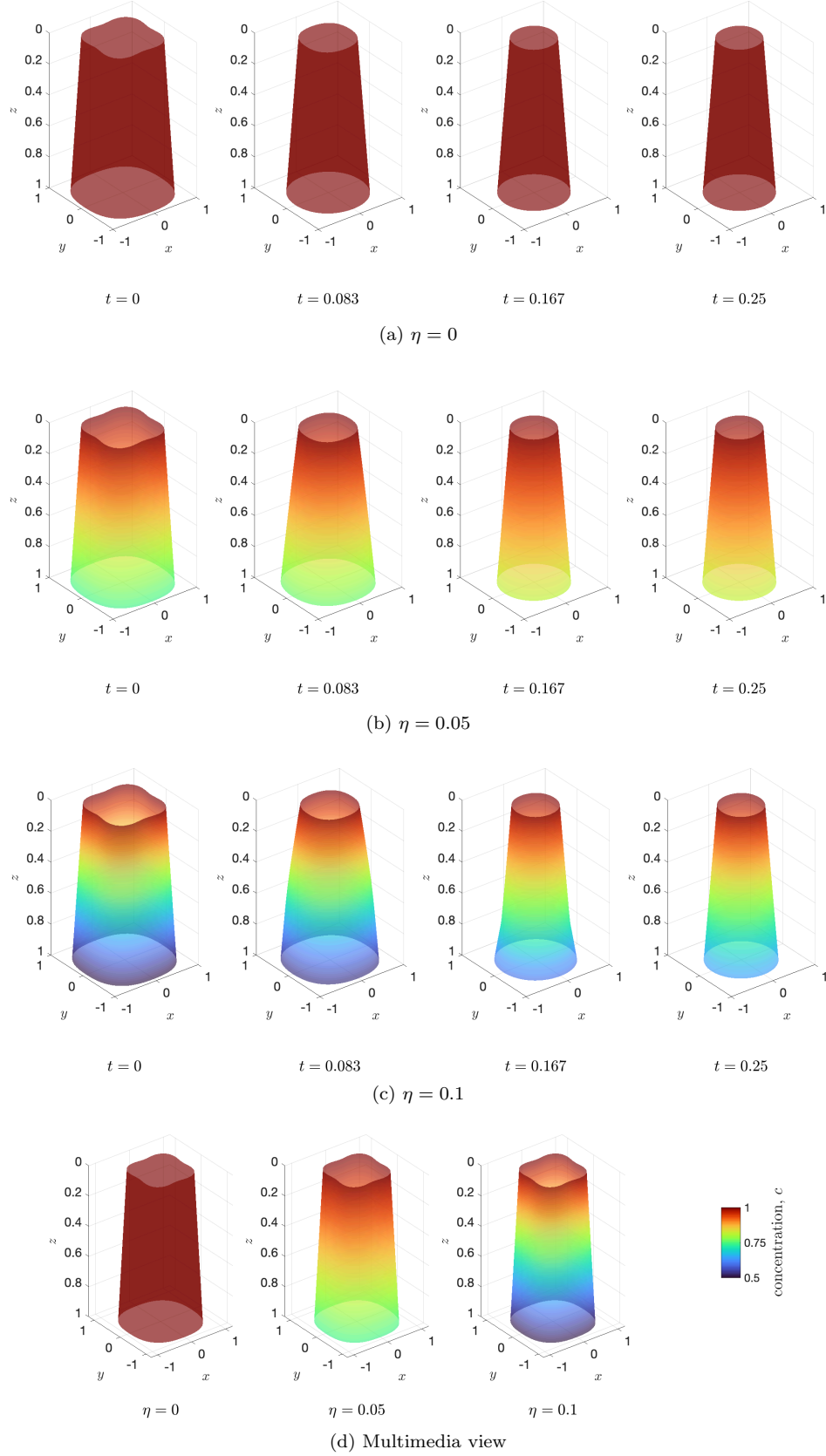


FIG. 4. (a)-(c) show the fluid-cell-layer interface  $a(\theta, z, t) = a_0(t) + \epsilon a_1(z, t) + \epsilon^2 (\Lambda_2(z, t) \cos(n\theta) + \Upsilon_2(z, t)) + O(\epsilon^3)$ , at different times with hunger rates  $\eta = 0, 0.05$  and  $0.1$ , respectively. Here,  $a_0(0) = 0.9$ ,  $a_1(z, 0) = z - 0.5$ ,  $\Lambda_2(z, 0) = -z + 2$ ,  $\Upsilon_2(z, 0) = -z + 2$ ,  $n = 4$ ,  $\epsilon = 0.2$  and  $Pe = 1$ .  $f$  is defined and graphed in (28) and Fig. 2 respectively, with  $m \rightarrow \infty$ . The colorbar shows the nutrient concentration. (d) provides more details on the pore evolution (Multimedia view).

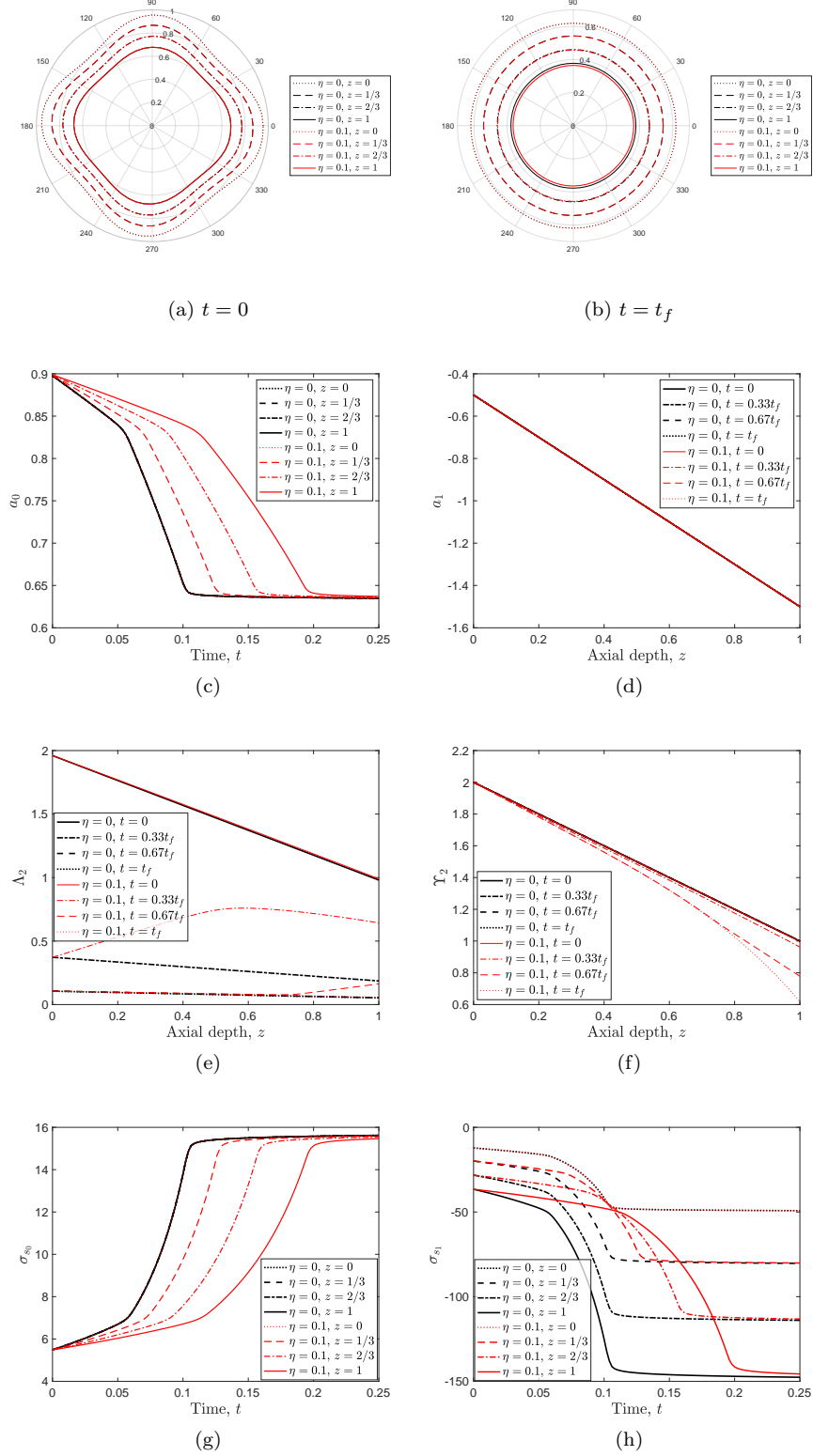


FIG. 5. (a) and (b) show the fluid-cell-layer interface  $a(\theta, z, t) = a_0(t) + \epsilon a_1(z, t) + \epsilon^2 (\Lambda_2(z, t) \cos(n\theta) + \Upsilon_2(z, t)) + O(\epsilon^3)$  at the initial and final ( $t_f$ ) time, respectively. (c)-(f) are profiles for  $a_0$ ,  $a_1$ ,  $\Lambda_2$  and  $\Upsilon_2$  respectively. (g) and (h) are  $\sigma_{s_0}$  and  $\sigma_{s_1}$  versus time, respectively. All graphs are for  $\eta = 0$  and  $\eta = 0.1$  as well as several different times and  $z$ . Here,  $a_0(0) = 0.9$ ,  $a_1(z, 0) = -z - 0.5$ ,  $\Lambda_2(z, 0) = -z + 2$ ,  $\Upsilon_2(z, 0) = -z + 2$ ,  $n = 4$ ,  $\epsilon = 0.2$  and  $\text{Pe} = 1$ .  $f$  is defined and graphed in (28) and Fig. 2 respectively, with  $m \rightarrow \infty$ .

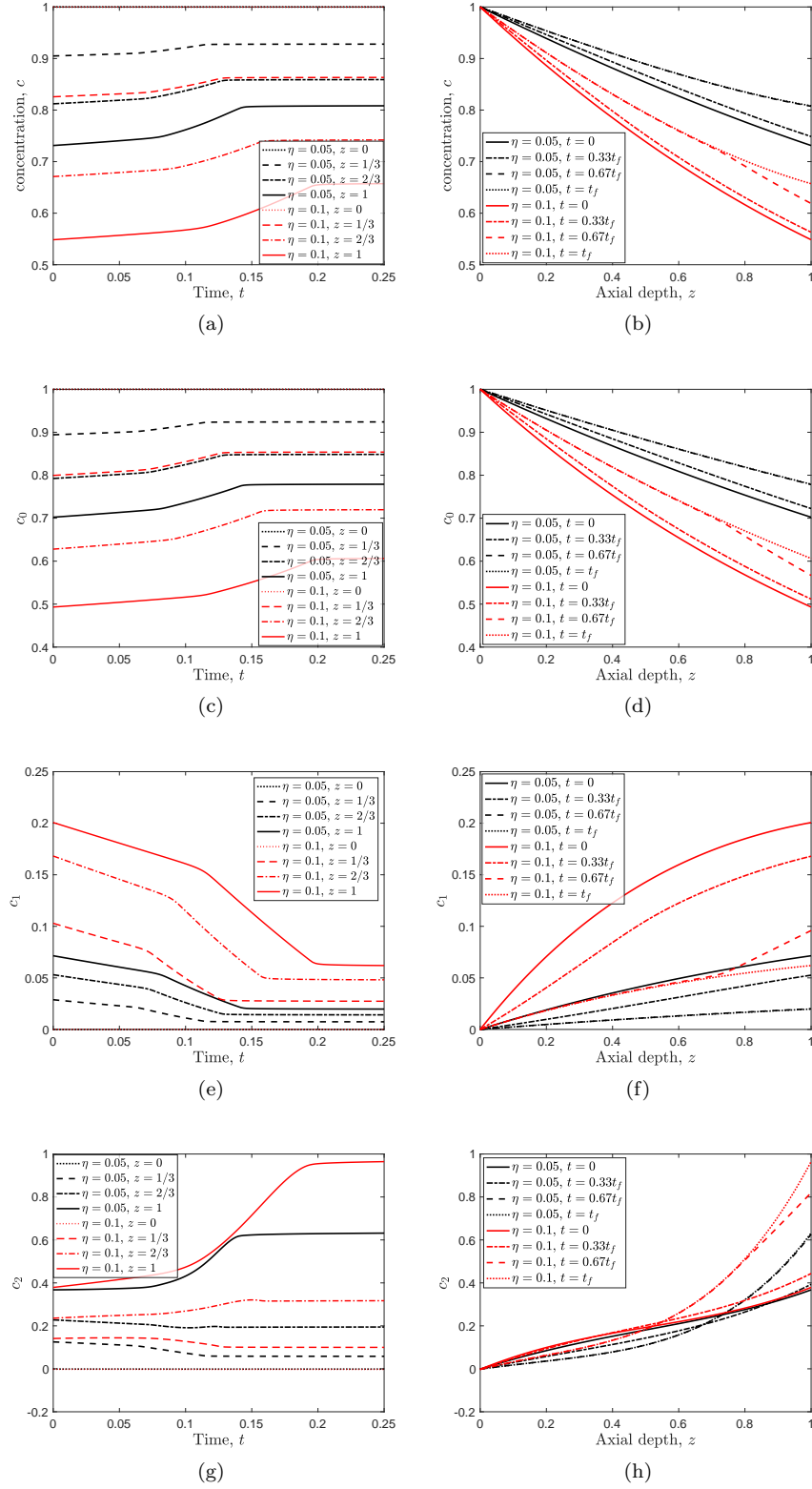


FIG. 6. Particle concentration profiles  $c$ ,  $c_0$ ,  $c_1$  and  $c_2$  versus  $t$  and  $z$  for  $\eta = 0.05$  and  $0.1$ . Here,  $a_0(0) = 0.9$ ,  $a_1(z, 0) = -z - 0.5$ ,  $\Lambda_2(z, 0) = -z + 2$ ,  $\Upsilon_2(z, 0) = -z + 2$ ,  $n = 4$ ,  $\epsilon = 0.2$  and  $\text{Pe} = 1$ .  $f$  is defined and graphed in (28) and Fig. 2 respectively, with  $m \rightarrow \infty$ .

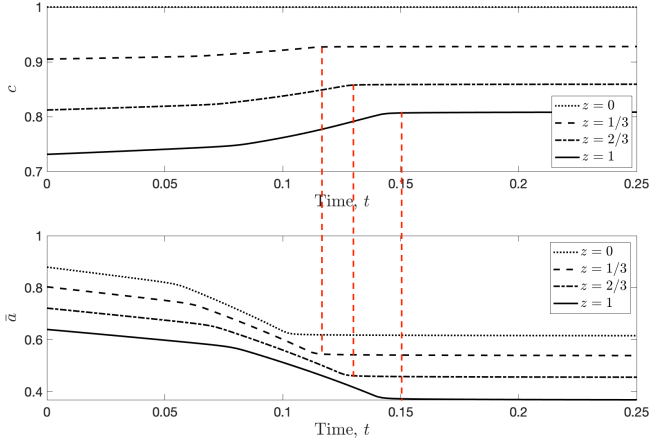


FIG. 7. Nutrient concentration and averaged radius of fluid-cell-layer interface defined as  $\bar{a}(z, t) = \frac{1}{2\pi} \int_0^{2\pi} a(z, t, \theta) d\theta$  versus time at several  $z$  for  $\eta = 0.05$ . Here,  $a_0(0) = 0.9$ ,  $a_1(z, 0) = -z - 0.5$ ,  $\Lambda_2(z, 0) = -z + 2$ ,  $\Upsilon_2(z, 0) = -z + 2$ ,  $n = 4$ ,  $\epsilon = 0.2$  and  $Pe = 1$ .  $f$  is defined and graphed in (28) and Fig. 2 respectively, with  $m \rightarrow \infty$ . The vertical red dotted lines are added to guide the eyes.

$z_0$  stops growing is demonstrated by the turning point where the average radius of fluid-cell interface defined as  $\bar{a}(z_0, t) = \frac{1}{2\pi} \int_0^{2\pi} a(z_0, t, \theta) d\theta$  stops to decrease and becomes flat. The average is introduced here because  $a$  has azimuthal variation with respect to  $\theta$ .

### C. Total tissue growth

We define the total tissue growth  $V(t)$  to be the total volume of the tissue growth within the pore at time  $t$ , *i.e.*

$$\begin{aligned} V(t) &= \int_0^1 \int_0^{2\pi} \int_{a(\theta, z, t)}^{a(\theta, z, 0)} r dr d\theta dz \\ &= \int_0^1 \int_0^{2\pi} \frac{1}{2} (a^2(\theta, z, 0) - a^2(\theta, z, t)) d\theta dz. \end{aligned} \quad (64)$$

Figures 8(a) and (b) show the total dimensionless tissue growth  $V(t)$  versus time  $t$ , for several different values of hunger rate  $\eta$  and the number of corners  $n$ , respectively. In §VB, we have already mentioned that a larger hunger rate  $\eta$  implies a longer incubation process and the same conclusion can be observed in Fig. 8(a). The incubation terminates when the curve for  $V(t)$  becomes flat. Notice that when  $\eta = 0.1$  this happens at around  $t = 0.2$ , and when  $\eta = 0.01$  this happens at around  $t = 0.1$ .

Recall that in §VA, we discussed the phenomena of a “sequential eating”. A smaller  $\eta$  (or even  $\eta = 0$ ) implies less sequential but more simultaneous proliferation. Correspondingly, one also observes that the slope of the total tissue growth curve  $V(t)$ , which reflects how fast the total tissue growth is accumulating, is smaller when  $\eta$  is higher, since simultaneous proliferation of all cells

(when  $\eta$  is smaller) yields faster tissue growth than sequential proliferation (when  $\eta$  is larger)<sup>19</sup>. Observe that, albeit tiny, the larger the hunger rate, the more total tissue growth the system can accumulate as shown in Fig. 8(a). This is straightforward to understand: as is stated above, when  $\eta$  is larger, it takes longer time for the system to terminate. So the total supply, and hence the total consumption, of nutrient is higher, yielding more tissue growth. We can conclude that cells with high hunger rate would yield profuse tissue growth in pore incubation.

Furthermore, in the work by Sanaei et al.<sup>14</sup> (or equivalently, when  $\eta = 0$  in our work), the total tissue growth is piece-wise linear. This occurs due to the piece-wise form of  $f$  (see (28)), when the shear stress reaches its threshold levels  $\sigma_1$  and  $\sigma_2$ . In the case when  $\eta = 0$ , cells at different tube depths experience the change of the value of the growth function  $f$  simultaneously, so the piece-wise linearity of  $f$  is preserved and inherited in the total tissue growth. While for  $\eta > 0$ , we see a more smooth total tissue curve, representing a more natural transition process. The growth rate is not uniform along the tube depth. The top cells proliferate first, the bottom cells then follow (as is evident in Figs. 3(d) and 4(d) (Multimedia view)). Our model “smooth out” the original total tissue growth curve, capturing the transition process, which is also introduced in Fig. 8(a).

Another observation is that  $n$  rarely influences the simulation results. In Fig. 8(b), we see that for different values of  $n$  (the number of lobes, which we take as a proxy for the shape of the underlying scaffold pore)<sup>14</sup>, the total tissue growth would remain the same as the proliferation terminates. Moreover, since the curves corresponding to different  $n$  collapse to exactly one curve, this also indicates that the rate of tissue accumulation would be the same for different  $n$  throughout the whole process. This observation is compatible with the one in the work by Sanaei et al.<sup>14</sup>, which reports that  $n$  does not influence total tissue growth without the dimension of concentration  $c$ . Therefore, the conclusion is the same when concentration is added.

### D. Scaffold design with respect to the final pore geometry

In laboratory environment, the researchers sometimes prescribe the final geometry of the desired tissue growth, and try to figure out an initial pore configuration so that the goal can be targeted. Our model provides a convenient guidance to how the pore should be designed, given the targeting tissue geometry. In this section, we propose an algorithm that can guide the pore design, and demonstrate how it can be used through several examples. Note that, the full advection-diffusion equation is a parabolic equation, therefore it is not reversible in time, but under quasi-static assumption, our system is time reversible<sup>31,37,38</sup>. Observe that the fluid dynamics for the nutrient flow would be the same in both the original and the reverse direction, hence, the only part that shall

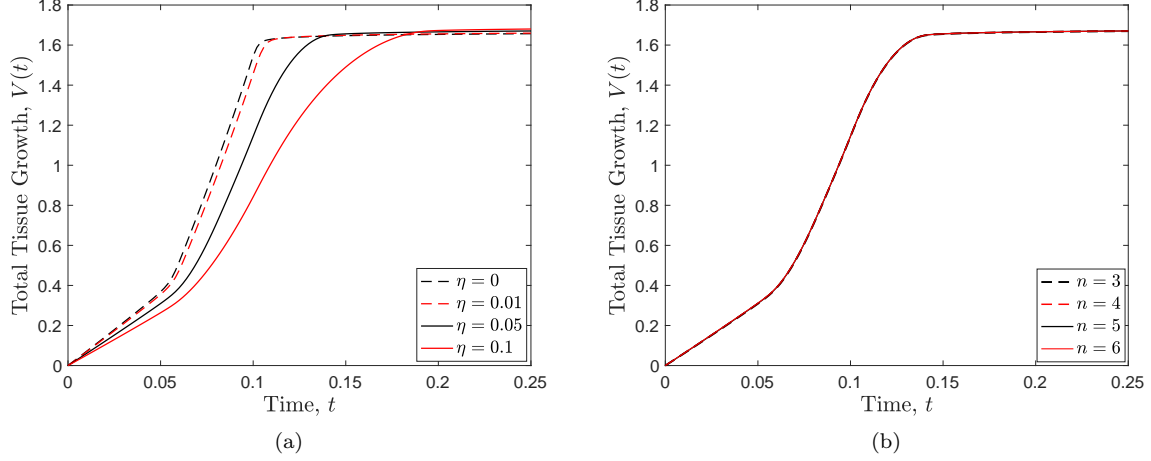


FIG. 8. (a) Total tissue growth  $V(t)$  versus time  $t$  for several different values of hunger rates  $\eta$ . Total tissue growth is defined as  $V(t) = \int_0^1 \int_0^{2\pi} \frac{1}{2} (a^2(\theta, z, 0) - a^2(\theta, z, t)) d\theta dz$ , or heuristically, the total volume occupied by tissue. Here,  $a_0(0) = 0.9$ ,  $a_1(z, 0) = -z - 0.5$ ,  $\Lambda_2(z, 0) = -z + 2$ ,  $\Upsilon_2(z, 0) = -z + 2$ ,  $n = 4$ ,  $\epsilon = 0.2$  and  $Pe = 1$ .  $f$  is defined and graphed in (28) and Fig. 2 respectively, with  $m \rightarrow \infty$ . (b) Total tissue growth versus time for different  $n$  with  $\eta = 0.05$ . Other parameters and initial conditions are chosen to be the same as in (a).

be modified is the tissue growth. Instead of the tissue proliferation, now the tissue would be shrinking, *i.e.*

$$\frac{\partial a}{\partial t} = +\kappa f(\sigma_s). \quad (65)$$

in dimensionless form and in contrast to (27).

Though one may want different radii for the final geometry, after parameters related to cell growth are prescribed, the final radius must fall in some feasible range, for if the radius is too small, shear stress would be too large to support cell growth, as is shown in the tail part of Fig. 2. Recall from (33) and (41) that  $\sigma_{s_0} = 4/a_0^3$ . As  $f(\sigma_s) = 0$  for  $\sigma_s > \sigma_2$ , in order for cells to grow, we must require  $\sigma_{s_0} \leq \sigma_2$ , otherwise the initial shear stress would be too large to support tissue growth. Therefore, the smallest possible final radius, which also corresponds to the largest possible volume of tissue growth, is precisely achieved when  $a_0 \geq (4/\sigma_2)^{(1/3)}$ .

It is efficient to have a scaffold pore structure resulting in a uniform final pore profile, meaning that the most part of the tube is being used for cells to proliferate. As a demonstration, we solve (65) for the initial scaffold pore design when the final geometry is uniform. As shown in Fig. 9(a) (see also Fig. 9(b) (Multimedia view)), we prescribe the final geometry, and run the algorithm to figure out the initial pore design, specifying different number of corners. The algorithm terminates when the pore radius does not increase. The uniformly circular black curves show the prescribed final geometry, and the red curves show the initial pore design calculated by our algorithm. We can see from the figure that when  $n$  is small, or with few corners, we can afford to have initial pore design with larger radius. Therefore, more total tissue growth is generated, when  $n$  is smaller, in other words, with more

corners, we get smaller initial pore design and less total tissue growth.

Another observation is that, to sustain a uniform final geometry, the initial pore must be designed in a funnel-like shape. The designed pore should be wider at the top of the tube at  $z = 0$  and gradually become thinner toward the bottom at  $z = 1$ . Since concentration is higher at the top, cell growth is faster at the top, therefore to achieve uniform final geometry, larger space is needed at the top to accommodate more tissue growth. This can be seen from Fig. 9 that in each graph, the dotted red curve, which corresponds to the initial pore design at the top of the tube, is wider than the solid red curve, which corresponds to the initial pore design at the bottom.

## VI. CONCLUSION

As a broad continuation of the model proposed by Sanaei et al.<sup>14</sup>, we present a more comprehensive and realistic mathematical model by including the fluctuation of nutrient concentration during proliferation. The flow of nutrient is captured by the Stokes' equation, with no-slip and no-penetration boundary conditions at the channel wall. The concentration of the flow is governed by the advection-diffusion equation for nutrient flux, with the effects of nutrient diffusion and fluid drift as a consequence of the flow interacting with pore wall, while the boundary condition of nutrient flux also depends on the ‘‘hunger rate’’ of the cells. The cell proliferation is modelled based on the nutrient concentration, curvature of cell-layer interface, as well as biological cell growth rule under fluid shear stress. The resulting equations are analyzed using asymptotic analysis (based on the small

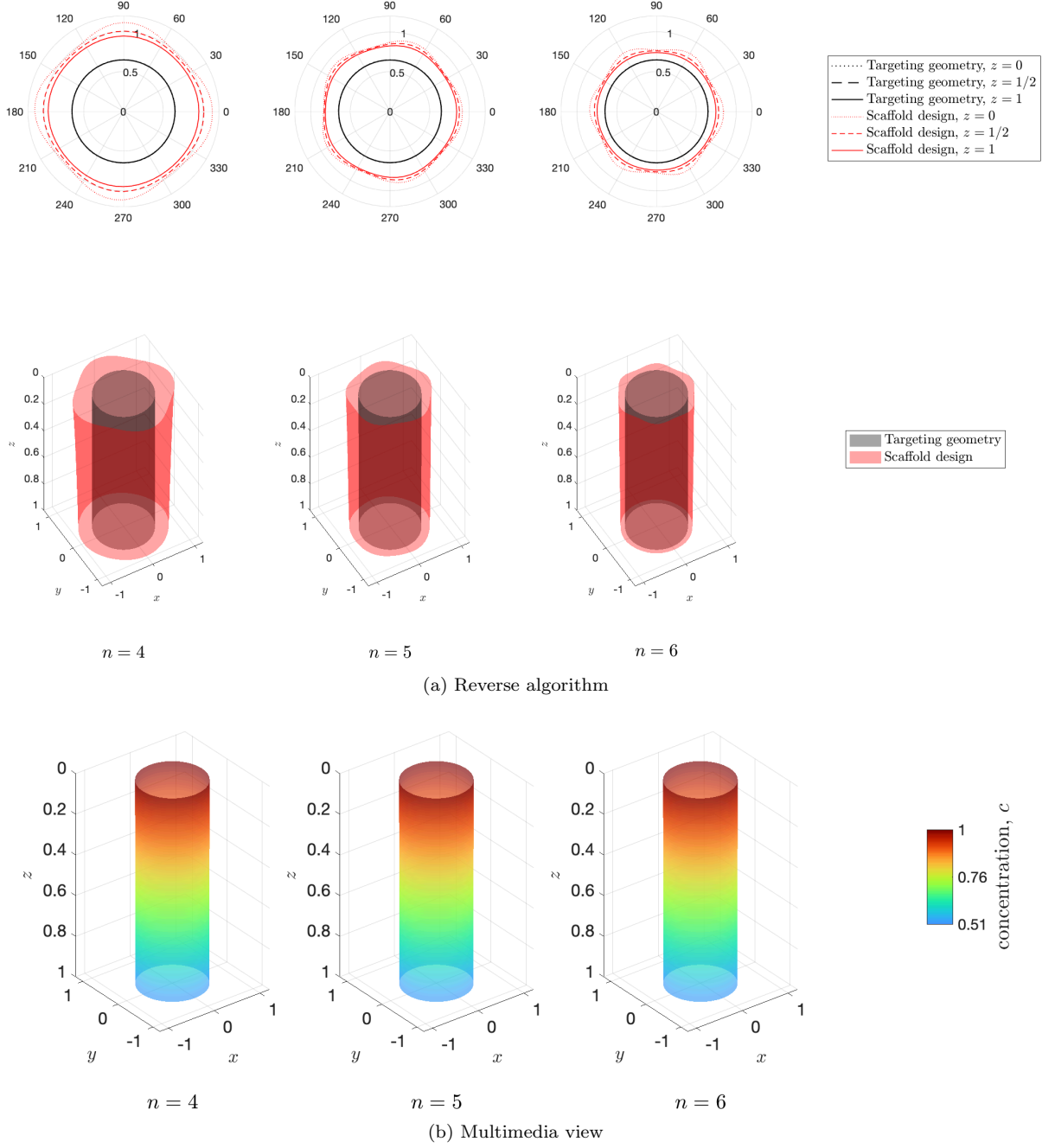


FIG. 9. Scaffold design with uniform final radius  $a(\theta, z, t_f) = 0.6$  for different values of the number of lobes  $n$ . Here,  $\epsilon = 0.2$ ,  $Pe = 1$ ,  $\eta = 0.1$ , and  $f$  is defined and graphed in (28) and Fig. 2 respectively, with  $m \rightarrow \infty$ . (b) provides more details on the reverse algorithm (Multimedia view).

aspect ratio of the pore as well as the expression for the fluid-cell-layer interface given in (29) and (30)), where we are able to determine the dominant equations for the nutrient concentration. With the assumption that the tissue growth happens on a much longer timescale than that associated with transport of fluid through the pore, we adopt the quasi-static assumption and update the rate of tissue growth based on the nutrient concentration. The

numerical simulation results from our extended model are compared with those from Sanaei *et al.*<sup>14</sup> which assumes the nutrient concentration is always constant along the pore depth. Our results also demonstrate consistency with experimental result from Rumpler *et al.*<sup>8</sup> as also reported in<sup>14</sup>.

Innovatively, our model includes a parameter representing the rates of nutrient consumption of different



cells. Our results show that a larger “hunger rate”  $\hat{\eta}$ , or in its dimensionless form  $\eta$ , yields longer incubation time, lower nutrient concentration, different final pore geometries, and more total tissue growth. Albeit the changes in the final pore geometry are rather small, the processes during which final geometries are achieved are noticeably different. With a higher hunger rate, pore geometry changes “sequentially” from top to bottom as time passes. With a lower or even zero hunger rate (representing almost excess or excess nutrient supply), top part and bottom part of the pore react almost simultaneously, without the sequential behaviour. Furthermore, we present a corresponding reverse algorithm which, given the targeting final pore geometry, can yield feasible initial scaffold pore designs. One simple example is discussed in this paper, but the algorithm can be practically applied to any final pore geometry to design an appropriate initial scaffold pore geometry.

Finally, in terms of future improvements, our model considers the homogeneous properties of cells while neglects the possible variants such as a changeable “hunger rate” when the environment varies<sup>19</sup>. Additionally, in this work, we do not consider the deformation of the scaffold. In reality, however, tissue is cultured in an elastic scaffold design. The tissue growth and shear stress may cause a slight deformation of the scaffold, thus affecting the overall growth process<sup>16</sup>. Nevertheless, our model and algorithm are practical and computationally efficient, providing a convenient tool to simulate tissue growth results and propose a scaffold design given desired tissue model outcome.

## Acknowledgements

The authors gratefully acknowledge support from the following sources: Z.Z. and X.L. from the Summer Undergraduate Research Experience offered by Courant Institute, New York University; P.S. from the National Science Foundation (NSF) under Grant No. RTG/DMS-1646339 and No. DMS-2108161 as well as an Institutional Support of Research and Creativity (ISRC) grant provided by New York Institute of Technology. The authors thank C. Peskin for useful discussions.

## Data Availability Statement

Data that support the findings of this study are available within the article. Further information is available from the corresponding author upon reasonable request.

<sup>1</sup>F. R. Rose and R. O. Oreffo, “Bone tissue engineering: hope vs hype,” *Biochemical and biophysical research communications* **292**, 1–7 (2002).

<sup>2</sup>I. Martin, D. Wendt, and M. Heberer, “The role of bioreactors in tissue engineering,” *TRENDS in Biotechnology* **22**, 80–86 (2004).

<sup>3</sup>M. Paris, A. Gutz, I. Hettrich, C. M. Bidan, J. W. Dunlop, H. Razi, I. Zizak, D. W. Huttmacher, P. Fratzl, G. N. Duda, and

et al., “Scaffold curvature-mediated novel biomineralization process originates a continuous soft tissue-to-bone interface,” *Acta Biomaterialia* **60**, 64â80 (2017).

<sup>4</sup>M. Mullender, A. El Haj, Y. Yang, M. Van Duin, E. Burger, and J. Klein-Nulend, “Mechanotransduction of bone cells in vitro: mechanobiology of bone tissue,” *Medical and Biological Engineering and Computing* **42**, 14–21 (2004).

<sup>5</sup>A. Bakker, J. Klein-Nulend, and E. Burger, “Shear stress inhibits while disuse promotes osteocyte apoptosis,” *Biochemical and biophysical research communications* **320**, 1163–1168 (2004).

<sup>6</sup>J. You, C. Yellowley, H. Donahue, Y. Zhang, Q. Chen, and C. Jacobs, “Substrate deformation levels associated with routine physical activity are less stimulatory to bone cells relative to loading-induced oscillatory fluid flow,” *J. Biomech. Eng.* **122**, 387–393 (2000).

<sup>7</sup>E. Gamsjager, C. M. Bidan, F. D. Fischer, P. Fratzl, and J. Dunlop, “Modelling the role of surface stress on the kinetics of tissue growth in confined geometries,” *Acta biomaterialia* **9**, 5531–5543 (2013).

<sup>8</sup>M. Rumppler, A. Woesz, J. W. Dunlop, J. T. Van Dongen, and P. Fratzl, “The effect of geometry on three-dimensional tissue growth,” *Journal of the Royal Society Interface* **5**, 1173–1180 (2008).

<sup>9</sup>C. M. Nelson, R. P. Jean, J. L. Tan, W. F. Liu, N. J. Sniadecki, A. A. Spector, and C. S. Chen, “Emergent patterns of growth controlled by multicellular form and mechanics,” *Proceedings of the National Academy of Sciences* **102**, 11594–11599 (2005).

<sup>10</sup>J. Wang, K. Lo, S. Chou, S. McCue, and M. T. Simpson, “The role of initial geometry in experimental models of wound closing,” *Chem. Eng. Sci.* **179**, 221â226 (2018).

<sup>11</sup>R. D. O’Dea, M. Nelson, A. El Haj, S. L. Waters, and H. M. Byrne, “A multiscale analysis of nutrient transport and biological tissue growth in vitro,” *Mathematical medicine and biology: a journal of the IMA* **32**, 345–366 (2015).

<sup>12</sup>R. ODea, H. Byrne, and S. Waters, “Continuum modelling of in vitro tissue engineering: a review,” *Computational Modeling in Tissue Engineering* **10**, 229–266 (2012).

<sup>13</sup>Y. Guyot, I. Papantoniou, Y. C. Chai, S. Van Bael, J. Schrooten, and L. Geris, “A computational model for cell/ecm growth on 3d surfaces using the level set method: a bone tissue engineering case study,” *Biomechanics and modeling in mechanobiology* **13**, 1361–1371 (2014).

<sup>14</sup>P. Sanaei, L. Cummings, S. Waters, and I. Griffiths, “Curvature- and fluid-stress-driven tissue growth in a tissue-engineering scaffold pore,” *Biomechanics and modeling in mechanobiology* **18**, 589–605 (2019).

<sup>15</sup>M. A. Alias and P. R. Buenzli, “Modeling the effect of curvature on the collective behavior of cells growing new tissue,” *Biophysical journal* **112**, 193–204 (2017).

<sup>16</sup>P. Kumar, B. Dey, and G. R. Sekhar, “Nutrient transport through deformable cylindrical scaffold inside a bioreactor: an application to tissue engineering,” *International Journal of Engineering Science* **127**, 201–216 (2018).

<sup>17</sup>P. Kumar and G. Raja Sekhar, “Analysis of elastohydrodynamics and nutrient transport through deformable porous scaffold inside a hollow fiber membrane bioreactor,” *Physics of Fluids* **32**, 031904 (2020).

<sup>18</sup>M. A. Alias and P. R. Buenzli, “A level-set method for the evolution of cells and tissue during curvature-controlled growth,” *International journal for numerical methods in biomedical engineering* **36**, e3279 (2020).

<sup>19</sup>S. G. Hegarty-Cremer, M. J. Simpson, T. L. Andersen, and P. R. Buenzli, “Modelling cell guidance and curvature control in evolving biological tissues,” *Journal of Theoretical Biology* **520**, 110658 (2021).

<sup>20</sup>F. Zhao, T. J. Vaughan, and L. M. McNamara, “Quantification of fluid shear stress in bone tissue engineering scaffolds with spherical and cubical pore architectures,” *Biomechanics and modeling in mechanobiology* **15**, 561–577 (2016).



- <sup>21</sup>S. M. Giannitelli, D. Accoto, M. Trombetta, and A. Rainer, "Current trends in the design of scaffolds for computer-aided tissue engineering," *Acta biomaterialia* **10**, 580–594 (2014).
- <sup>22</sup>A. Cheng, Z. Schwartz, A. Kahn, X. Li, Z. Shao, M. Sun, Y. Ao, B. D. Boyan, and H. Chen, "Advances in porous scaffold design for bone and cartilage tissue engineering and regeneration," *Tissue Engineering Part B: Reviews* **25**, 14–29 (2019).
- <sup>23</sup>A. Rouhollahi, O. Ilegbusi, S. Florczyk, K. Xu, and H. Foroosh, "Effect of mold geometry on pore size in freeze-cast chitosan-alginate scaffolds for tissue engineering," *Annals of biomedical engineering* **48**, 1090–1102 (2020).
- <sup>24</sup>J. L. Drury and D. J. Mooney, "Hydrogels for tissue engineering: scaffold design variables and applications," *Biomaterials* **24**, 4337–4351 (2003).
- <sup>25</sup>N. C. Pearson, R. J. Shipley, S. L. Waters, and J. M. Oliver, "Multiphase modelling of the influence of fluid flow and chemical concentration on tissue growth in a hollow fibre membrane bioreactor," *Mathematical medicine and biology: a journal of the IMA* **31**, 393–430 (2014).
- <sup>26</sup>M. Shakeel, P. C. Matthews, R. S. Graham, and S. L. Waters, "A continuum model of cell proliferation and nutrient transport in a perfusion bioreactor," *Mathematical medicine and biology: a journal of the IMA* **30**, 21–44 (2013).
- <sup>27</sup>C. Chung, C. Chen, C. Chen, and C. Tseng, "Enhancement of cell growth in tissue-engineering constructs under direct perfusion: Modeling and simulation," *Biotechnology and bioengineering* **97**, 1603–1616 (2007).
- <sup>28</sup>G. Lemon, J. R. King, H. M. Byrne, O. E. Jensen, and K. M. Shakesheff, "Mathematical modelling of engineered tissue growth using a multiphase porous flow mixture theory," *Journal of mathematical biology* **52**, 571–594 (2006).
- <sup>29</sup>G. I. Taylor, "Dispersion of soluble matter in solvent flowing slowly through a tube," *Proceedings of the Royal Society of London. Series A. Mathematical and Physical Sciences* **219**, 186–203 (1953).
- <sup>30</sup>P. Sanaei and L. J. Cummings, "Flow and fouling in membrane filters: effects of membrane morphology," *Journal of Fluid Mechanics* **818**, 744 (2017).
- <sup>31</sup>S. Y. Liu, Z. Chen, and P. Sanaei, "Effects of particles diffusion on membrane filters performance," *Fluids* **5**, 121 (2020).
- <sup>32</sup>K. P. Kommareddy, C. Lange, M. Rumpler, J. W. Dunlop, I. Manjubala, J. Cui, K. Kratz, A. Lendlein, and P. Fratzl, "Two stages in three-dimensional in vitro growth of tissue generated by osteoblastlike cells," *Biointerphases* **5**, 45–52 (2010).
- <sup>33</sup>R. D. O'Dea, S. L. Waters, and H. M. Byrne, "A multiphase model for tissue construct growth in a perfusion bioreactor," *Mathematical medicine and biology: a journal of the IMA* **27**, 95–127 (2010).
- <sup>34</sup>R. J. Shipley and S. L. Waters, "Fluid and mass transport modelling to drive the design of cell-packed hollow fibre bioreactors for tissue engineering applications," *Mathematical medicine and biology: a journal of the IMA* **29**, 329–359 (2012).
- <sup>35</sup>H. Suhaimi and D. B. Das, "Glucose diffusivity in cell-seeded tissue engineering scaffolds," *Biotechnology letters* **38**, 183–190 (2016).
- <sup>36</sup>R. J. McMurtrey, "Analytic models of oxygen and nutrient diffusion, metabolism dynamics, and architecture optimization in three-dimensional tissue constructs with applications and insights in cerebral organoids," *Tissue Engineering Part C: Methods* **22**, 221–249 (2016).
- <sup>37</sup>M. P. Dalwadi, M. Bruna, and I. M. Griffiths, "A multiscale method to calculate filter blockage," *Journal of Fluid Mechanics* **809**, 264–289 (2016).
- <sup>38</sup>M. P. Dalwadi, I. M. Griffiths, and M. Bruna, "Understanding how porosity gradients can make a better filter using homogenization theory," *Proceedings of the Royal Society A: Mathematical, Physical and Engineering Sciences* **471**, 20150464 (2015).
- <sup>39</sup>C. M. Bidan, K. P. Kommareddy, M. Rumpler, P. Kollmannsberger, P. Fratzl, and J. W. Dunlop, "Geometry as a factor for tissue growth: towards shape optimization of tissue engineering scaffolds," *Advanced healthcare materials* **2**, 186–194 (2013).